Research Article Vol. 31, No. 21 / 9 Oct 2023 / *Optics Express* 34428

Optics EXPRESS

Generalizing amplitude swing modulation for versatile ultrashort pulse measurement

MIGUEL LÓPEZ-RIPA, ÍÑIGO J. SOLA, AND BENJAMÍN ALONSO*

Grupo de Investigación en Aplicaciones del Láser y Fotónica, Departamento de Física Aplicada, Universidad de Salamanca, Salamanca, E-37008, Spain
**b.alonso@usal.es*

Abstract: In this work we broaden the amplitude modulation concept applied to the temporal characterization of ultrashort laser pulses with the amplitude swing technique. We theoretically study the effect of diverse types of relative amplitude and phase modulations. This variation of the replicas can be implemented by means of rotating zero-order waveplates to manipulate the delayed pulse replicas produced in a following multi-order waveplate, which can be more practical under certain conditions. We numerically simulate and study different scenarios under different modulations and for different noise levels and pulses. The proposed schemes are validated and compared through the experimental application to compressed and chirped pulses, confirming the applicability of the work. The simplicity, robustness and versatility of this ultrashort pulse measurement benefits the applications of ultrafast optics.

1. Introduction

There is a high number of applications of ultrashort laser pulses, for example, microprocessing [1], nonlinear microscopy [2], nano-structuring of materials [3], or laser structuring in biomedical applications [4], among many others. In the last decades, it has been shown that the applications of ultrafast optics have been growing hand in hand with the tools available for their characterization [5,6]. The extremely brief duration and rapid oscillation of the electric field in ultrashort pulses, make their measurement a challenging task. Many different strategies have been followed for this purpose, some of them giving partial information of the pulses, as nonlinear autocorrelation [7] in its different forms. Other techniques can measure the amplitude and phase of the pulses (i.e., resolving the pulse chirp), for example, spectral phase interferometry for direct electric-field reconstruction (SPIDER) [8], frequency-resolved optical gating (FROG) [9], self-referenced spectral interferometry [10], multiphoton intrapulse interference phase scan (MIIPS) [11], or dispersion scan (d-scan) [12]. Those techniques have evolved into different variants that present experimental advantages or improve the pulse reconstructions, such as interferometric autocorrelation [13], polarization-gate FROG [14], spatially encoded arrangement SPIDER [15], cross-polarized wave generation d-scan [16], among other examples [5,17]. More recently, other strategies have been developed, as tunneling ionization with a perturbation for the time-domain observation of an electric field (TIPTOE) [18] or femtosecond streaking through transient currents in air plasma [19]. Often, these temporal diagnostics are based on complex setups, for example, involving one or more interferometers [9,20] that require careful alignment and may be affected by instabilities. Also, the elements required for the pulse measurement are frequently very restrictive in terms of the pulse bandwidth, pulse chirp or spectral region of the pulse that can be characterized [21–25]. For this reason, it is convenient to have new techniques that can characterize the pulses with more straightforward and more versatile schemes, so that the process of pulse measurement is simplified, which benefits the ultrafast lasers community and the applications of the technology.

#500271 https://doi.org/10.1364/OE.500271
Journal © 2023 Received 11 Jul 2023; revised 14 Sep 2023; accepted 15 Sep 2023; published 29 Sep 2023

Recently, the amplitude swing technique [26] was introduced, which is a remarkably simple way to accomplish the task. Conceptually, it consists of creating two replicas of the input pulse with a constant delay and varying their relative amplitude, while measuring the spectrum of the second harmonic generation (SHG) signal they produce, resulting in the amplitude swing trace. From the experimental side, one of the key advantages of the first proposed setup is its compact implementation: the pulse replicas are generated and manipulated by rotating a multi-order waveplate (MWP) —e.g., a plane-parallel retarder plate consisting in a uniaxial crystal with appropriate thickness and birefringence— followed by a linear polarizer, before the SHG. This simple implementation with a bulk interferometer confers the system ultra-high stability and avoids the requirement of careful alignment of a standard interferometer. The technique has been demonstrated to be very robust in terms of tolerance to noise and to different parameters of the pulse manipulation (e.g., phase retardation or delay), as well as non-flat or clipped SHG response [27]. Recently, the versatility of the technique has been used to measure pulses in different spectral regions from the visible to the near infrared with the same setup [28] and it has been shown its capability to measure vector pulses [29]. The compactness and stability allow it to be integrated in other detection systems [30].

The potential of the technique [27–29] has led us to explore the implications of new modulations of the pulse replicas in the technique. In this work we propose to achieve it by introducing different modulations affecting not only the relative amplitude of the pulse replicas, but also their relative phase. From a theoretical point of view, we propose a configuration in which a rotating zero-order waveplate (ZWP) before a static MWP introduces the replicas modulation, which keeps the simplicity of conventional amplitude swing. We analyse the amplitude and phase variations, and, through defined modulation factors, we study the influence of the phase retardation of the ZWP to encode the pulse phase (then focusing on the cases of half- and quarter-waveplate retarders, HWP and QWP, respectively), finding high flexibility except for values close to zero or complete wave. We find that different phase retardations led to diverse types of amplitude and phase modulations, which are quantified and assessed. Through numerical simulations, we evaluate the performance of the new configurations compared to the original amplitude swing, finding that the new ones (scanning ZWP before a static MWP) can perform the task and it is in general more robust. Then, we show the experimental demonstration of the new configurations by measuring ultrashort pulses with different chirps. In particular, we show the experimental measurements with standard commercial elements that can be found in the laboratory, i.e., HWP and QWP retarders.

In the Discussion section, we provide a perspective of the work and deepen the advantages of the configuration proposed here in the scope of pulse characterization, e.g., more robustness, several independent measurements or ease the applicability of the technique.

2. Results

2.1. *Theoretical analysis of the generalizing amplitude modulation*

In the original implementation of amplitude swing [26] (rotating MWP), the input pulse was linearly polarized at 0°, then the MWP was rotated about the optical axis of the system, and the generated replicas were projected with a linear polarizer at 0°, so they interfere and can produce SHG in a type-I crystal. The resulting detected SHG signal $S_M(\omega, \theta_M)$ —the amplitude swing trace— is given by

$$S_M(\omega, \theta_M) = \left| \int \left(\int A(\omega') e^{i\phi_P(\omega')} [e^{i\phi_f(\omega')} \cos^2\theta_M + e^{i\phi_s(\omega')} \sin^2\theta_M] e^{i\omega' t} d\omega' \right)^2 e^{-i\omega t} dt \right|^2 \quad (1)$$

where the angular frequency is ω, the time t, the angle between the fast axis of the MWP and the horizontal axis is θ_M, the amplitude $A(\omega)$ and phase $\phi_P(\omega)$ of the electric field of the pulse to be measured, and the phase introduced by the fast $\phi_f(\omega)$ and slow $\phi_s(\omega)$ axes of the MWP. The delay between the pulse replicas comes from the fast and slow axes birefringence (the plate thickness is chosen so that the delay is of the order of the Fourier-limit of the spectrum), while the amplitude modulation of the replica comes from the rotating angle θ_M that is scanned between 0 and 180°.

2.1.1. Generalizing amplitude swing modulation: rotating ZWP before a static MWP

In the implementation proposed here, the input pulse is linearly polarized at 0°, then a ZWP is rotated between 0 and 180° (angle θ_Z between the fast axis of the ZWP and the x-axis) before a static MWP (fast axis at 45°), while a linear polarizer at 0° projects the modulated two replicas (the scheme of the setup is represented in Fig. 1) before the SHG. In this case, the expression for the amplitude swing trace, $S_Z(\omega,\theta_Z)$, is as follows

$$S_Z(\omega,\theta_Z) = \left|\int\left(\int A(\omega')e^{i\phi_P(\omega')}[e^{i\phi_f(\omega')}G_f(\theta_Z,\phi_r) + e^{i\phi_s(\omega')}G_s(\theta_Z,\phi_r)]e^{i\omega' t}d\omega'\right)^2 e^{-i\omega t}dt\right|^2 \tag{2}$$

where ϕ_r is the phase retardation of the ZWP (relative phase of slow to fast axis), and the functions $G_f(\theta_Z,\phi_r)$ and $G_s(\theta_Z,\phi_r)$ account for the modulation introduced to the fast and slow pulse replicas, respectively. These functions can be calculated from Jones calculus and, after simplification, can be expressed as (see demonstration in Supplement 1, Section 1)

$$\begin{aligned} G_f(\theta_Z,\phi_r) &= {}^1\!/_4(1+cos2\theta_Z+sin2\theta_Z) + {}^1\!/_4(1-cos2\theta_Z-sin2\theta_Z)e^{i\phi_r} \\ G_s(\theta_Z,\phi_r) &= {}^1\!/_4(1+cos2\theta_Z-sin2\theta_Z) + {}^1\!/_4(1-cos2\theta_Z+sin2\theta_Z)e^{i\phi_r} \end{aligned} \tag{3}$$

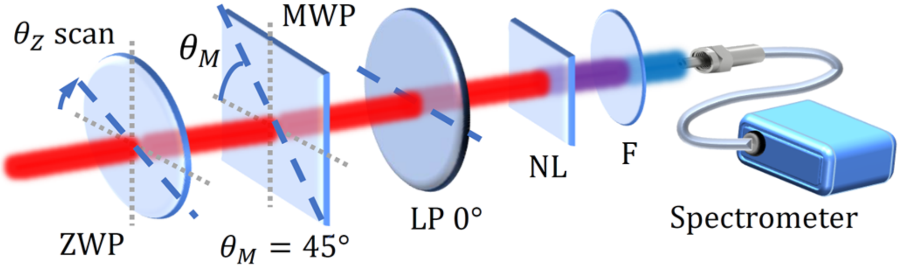

Fig. 1. Experimental setup. Scheme of the amplitude swing implemented with a rotating ZWP followed by a static MWP (45°) to create the pulse replicas, which are projected with a linear polarizer (LP) at 0°. Then, the SHG is generated in a nonlinear crystal (NL), the remaining fundamental signal is removed with a filter (F) and the SHG is measured with a spectrometer.

The difference between $S_Z(\omega,\theta_Z)$ (Eq. (2)) and $S_M(\omega,\theta_M)$ (Eq. (1)) is, precisely, the expression for the modulation factors. While in $S_M(\omega,\theta_M)$ the energy oscillates between the fast and slow pulse replicas while varying θ_M (pure amplitude modulation), in the case of $S_Z(\omega,\theta_Z)$ the modulation functions are complex (amplitude and phase) and depend on the phase retardation of the ZWP. Therefore, in the general case, the slow and the fast replica will have a varying relative phase, $\phi_{G_s-G_f}$, that can be obtained from the complex phase argument as (notice that we study the relative phase, since a global phase offset does not affect the trace):

$$\phi_{G_s-G_f}(\theta_Z,\phi_r) = arg[(1+cos4\theta_Z+2cos\phi_r sin^2 2\theta_Z) + i(4cos\theta_Z sin\theta_Z sin\phi_r)] \tag{4}$$

2.1.2. Quantification of the replica modulation and phase encoding

As shown, the amplitude variation introduced while scanning the angle θ_Z depends on the phase retardation ϕ_r of the ZWP. In the proposed configuration, both, the amplitude and phase of the modulated replica, are varied while scanning, so that we quantify the amount of modulation to evaluate the validity of the approach. In Fig. 2, we show the amplitude modulation ($|G_f|$ and $|G_s|$, absolute value in Eq. (3)) for the particular cases of the ZWP operation as a HWP ($\phi_r = \pi$) and a QWP ($\phi_r = \pi/2$), while in the Visualization 1 we show the variations for every ϕ_r. We find that for phase retardations close to π, the amplitude variation is maximum, each replica reaching zero for certain values of θ_Z. Moving away from that value, the amplitude modulation regularly becomes lower. Defining the contrast as $[max(|G|) - min(|G|)]/max(|G|)$ for each θ_Z, we find the amplitude contrast varies from 100% (for HWP) to 42% (for QWP), and to 0% (for complete wave retardation, i.e., $\phi_r = 0$ or 2π). Regarding the phase modulation $\phi_{G_s - G_f}$ (Eq. (4)), for HWP it is 0 or $\pm\pi$ in different θ_Z scan regions, while for other values of ϕ_r, the replicas dephase $\phi_{G_s - G_f}$ oscillates between $\pm\phi_r$. This means that, depending on ϕ_r, there is a relevant phase modulation (combined with said amplitude modulation), except for the case of complete wave retardation, which is a trivial case (the ZWP does not play any role) without modulation at all. To have a significant amplitude and phase modulation, with the present analysis (see the complete details in Supplementary Fig. 1 and 2) we find that using a ZWP with $\pi/2 \leq \phi_r \leq 3\pi/2$ ensures having a contrast above 40% and a relative phase variation above π. We have chosen that range since it presents a remarkable amplitude and phase modulation and comprises the cases of using QWP and HWP in the role of the rotating ZWP. Nevertheless, this is not a strict condition, but we have set these flexible limits as a conservative estimation to guarantee pulse phase encoding.

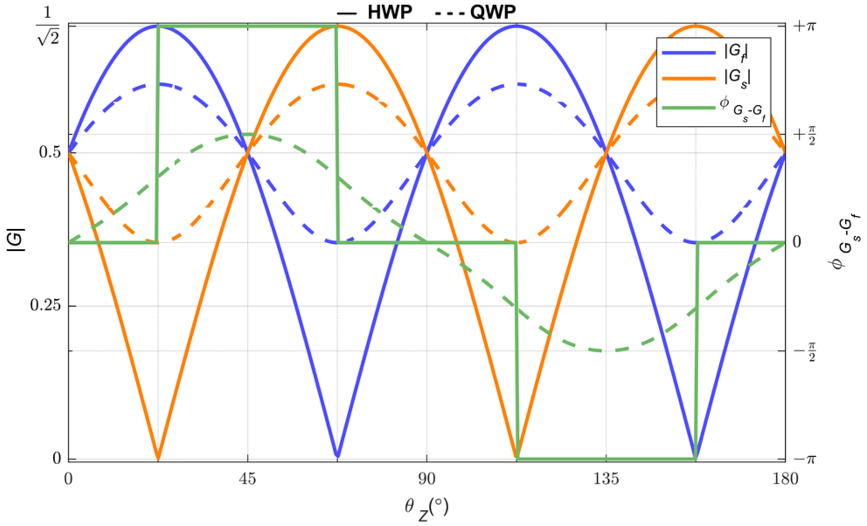

Fig. 2. Amplitude modulation for HWP and QWP cases. Fast (blue) and slow (orange) amplitude modulation ($|G_f|$ and $|G_s|$, respectively), and relative phase $\phi_{G_s - G_f}$ (green) variation during the ZWP scan in θ_Z, for the cases of HWP (solid) and QWP (dashed line). See in Visualization 1 for all possible phase retardations.

To corroborate the pulse phase encoding in the traces, we have simulated the traces for different situations where the ZWP introduces $\phi_r = 0.5\pi$, 0.75π, and π, and for comparison we also show the rotating MWP case. We consider 50-fs Fourier-limit gaussian pulses centred at 800 nm and a 60-fs delay MWP (2-mm quartz). For the MWP, we define as ϕ_M the phase retardation for the central wavelength (notice that for the MWP it is wavelength dependent), here we will simulate two examples with $\phi_M = \pi$ and $\phi_M = \pi/2$, without lack of generality for our purpose. For different pulses with $TOD = 0$ and ± 200000 fs^3 (third-order dispersion), combined with GDD ranging from 0 to 10000 fs^2 (group delay dispersion), the amplitude swing traces are shown in Supplementary Fig. 3 and Visualization 2, Visualization 3, Visualization 4, Visualization 5, Visualization 6, Visualization 7 (the full details are in Supplement 1, Section 3). As expected, it is found that the traces are sensitive to the pulse dispersion.

Finally, for the pulse used in Supplementary Fig. 3 (GDD = 4000 fs^2 and TOD = 200000 fs^3) and for $\phi_M = \pi$, we calculate the amplitude swing trace for different phase retardations ϕ_r from 0 to 2π (Visualization 8). We can conclude that for $\phi_r \neq 0$ or 2π, there is a relative amplitude and phase modulation of the replica, both contributing to the pulse phase encoding in amplitude swing trace, from which the pulse can be reconstructed.

2.1.3. Implementation with a rotating HWP

A case of particular interest, both from the theoretical and the experimental side, is when the ZWP corresponds to a HWP, then $\phi_r = \pi$. The amplitude modulation (see in Fig. 2) functions can be simplified to

$$\begin{aligned} G_f(\theta_Z, \pi) &= {}^1\!/_2(cos2\theta_Z + sin2\theta_Z) = {}^1\!\Big/\sqrt{2}cos(2\theta_Z - \pi/4) \\ G_s(\theta_Z, \pi) &= {}^1\!/_2(cos2\theta_Z - sin2\theta_Z) = -{}^1\!\Big/\sqrt{2}sin(2\theta_Z - \pi/4) \end{aligned} \tag{5}$$

In this case, the HWP rotates the orientation of the input linear polarization that is decomposed on the MWP axes. As the HWP rotates, there is a pure amplitude modulation of the replicas. This resembles the original scan (Eq. (1)) —in which the fast and slow replicas are modulated by $G_{fM}(\theta_M) = cos^2(\theta_M)$ and $G_{sM}(\theta_M) = sin^2(\theta_M)$, respectively— being the main difference that, since the MWP is static with respect to the LP in the rotating ZWP configuration, the cosine and sine projections are non-squared here (Eq. (2) and (5)). Other differences here are that the modulation oscillates with $2\theta_Z$ (instead of θ_M) and that there is shift in the trace due to the term $\pi/4$ in Eq. (5), both being due to the effect of the HWP rotating the input polarization before the MWP.

Consequently, the trace is repeated twice during the 180° scan in θ_Z (while for the original amplitude swing, the trace is symmetrical with respect to 90°). All the same, here there are also scan positions with only one replica and positions with balanced (equal amplitude) replicas (so that the contrast between the replicas in the rotating HWP varies from 0 to 100% as in the rotating MWP case), the balanced positions having here more signal than in the common implementation (each replica has 50% —instead of 25%— of its peak intensity), which benefit the signal to noise ratio in the interfering region of the trace. Also, there is a 0 or π phase difference between the fast and slow replicas depending on θ_Z, which comes from the replicas having the same or opposite sign during the amplitude modulation. Notice that this relative phase is added to the phase retardation due to the later static MWP. Altogether, it means that the trace scanning with a rotating HWP before the static MWP contains information that is equivalent to measuring two conventional traces with a rotating MWP, the first of them corresponding to the same MWP (used as static in the rotating HWP measurement) and the second one also with the same MWP but with a π dephase added to its phase retardation. In Supplement 1, Section 4 we include the detailed demonstration that leads to two transformations. The first one is a reshaping of the data in the original HWP trace, which comes from the condition that the relative amplitude of the two replicas is the same, giving the following relation between the θ_Z scan angle of the rotating HWP and the θ_M scan angle of the rotating MWP

$$\theta_Z = \begin{cases} mod\left(\frac{\pi}{8} + \frac{arctan(\mp tan^2(\theta_M))}{2}; \pi\right), \; for\ \theta_M \in [0, {}^{\pi}\!/_2) \\ mod\left(\frac{\pi}{8} + \frac{arctan(\mp tan^2(\theta_M)) + \pi}{2}; \pi\right), \; for\ \theta_M \in [{}^{\pi}\!/_2, \pi) \end{cases} \tag{6}$$

where the $\mp$ sign accounts for the case of obtaining the MWP trace with its actual phase retardation (upper case, − sign), and the MWP trace with the π dephase added (lower case, + sign). The function $mod(a;b)$ returns the remainder after division of a and b. The second transformation is a rescaling function of the data for different angles θ_M, which arises from imposing the condition that the global intensity of the pulse during the modulation and SHG is the same than in a rotating MWP trace, and is given by the expression

$$R(\theta_M) = \left(\frac{cos^2(\theta_M)}{cos(2\theta_Z - \pi/4)} \right)^4 \tag{7}$$

where θ_Z is given by Eq. (6). Both, reshaping and rescaling relations, are represented in Supplementary Fig. S5. These transformations are corroborated with simulated (Supplementary Fig. S6 and Visualization 9) and experimental (Supplementary Fig. S7) data.

Here, we show an experimental example of this situation (Fig. 3). For the chirped pulse that we will reconstruct in the Experimental measurements section, we measured the amplitude swing trace with a rotating MWP (phase retardation $\phi_M = 0.34\pi$) and with a rotating HWP before the same static MWP, the traces are shown in Fig. 3(a,b), respectively. As discussed, from the HWP trace, we use the transformation described here to calculate the MWP trace (Fig. 3(c)), which corresponds to the one that was directly measured (Fig. 3(a)). Moreover, the information of the HWP trace (Fig. 3(b)) allows us to calculate a second MWP trace but that corresponds to a phase retardation of $\phi_M + \pi$ in the MWP (Fig. 3(d)), which is not directly obtained experimentally with the rotating plate and can be considered as extra information.

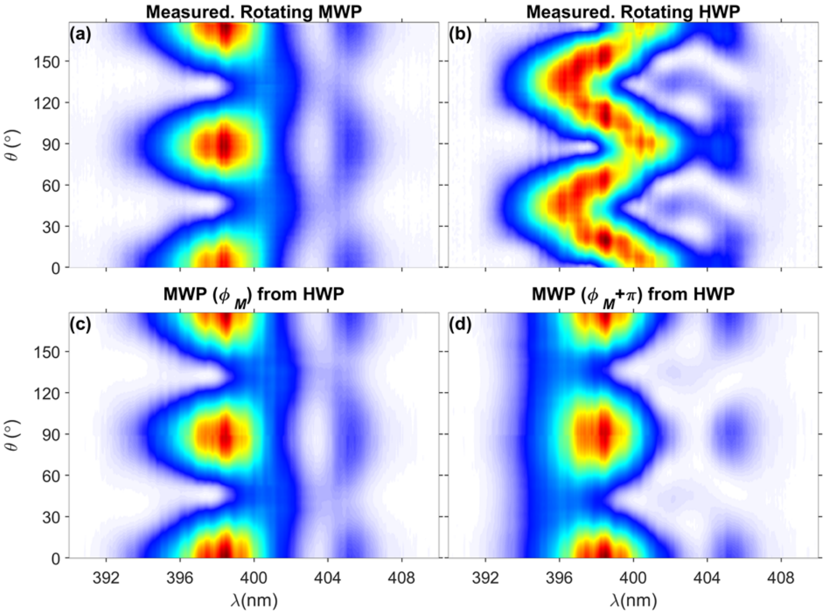

Fig. 3. Conversion of experimental HWP to MWP traces. Measured a MWP and b HWP trace with $\phi_M = 0.34\pi$. Calculated MWP trace with c $\phi_M = 0.34\pi$ and d $\phi_M = 1.34\pi$ from the HWP trace in b. The measures trace in a corresponds to the chirped pulse that we will reconstruct in the Experimental measurements section.

2.1.4. Implementation with a rotating QWP

Another case of interest from the experimental point of view is when the ZWP corresponds to a QWP, then $\phi_r = \pi/2$. Also, from the theoretical side, it allows us to explore in detail a case with both amplitude and phase modulation during the scan in θ_Z. In this situation, the modulation functions simplify to

$$\begin{aligned} G_f\left(\theta_Z, {}^{\pi}/_{2}\right) &= {}^{1}/_{4}\left(1 + cos2\theta_Z + sin2\theta_Z\right) + {}^{1}/_{4}\left(1 - cos2\theta_Z - sin2\theta_Z\right) i \\ G_s\left(\theta_Z, {}^{\pi}/_{2}\right) &= {}^{1}/_{4}\left(1 + cos2\theta_Z - sin2\theta_Z\right) + {}^{1}/_{4}\left(1 - cos2\theta_Z + sin2\theta_Z\right) i \end{aligned} \tag{8}$$

Contrarily to the HWP case, the amplitude modulation of the pulse replicas here is complex. To analyse and understand the effect of the modulations, we study their absolute value (amplitude) and their relative phase. The amplitude modulation is given by (the approximation below is done only to ease the interpretation, not for calculating purposes)

$$\begin{aligned} \left|G_f\left(\theta_Z, {}^{\pi}/_{2}\right)\right| &= {}^{1}/_{2}\sqrt{1 + {}^{1}/_{2} sin4\theta_Z} \\ \left|G_s\left(\theta_Z, {}^{\pi}/_{2}\right)\right| &= {}^{1}/_{2}\sqrt{1 - {}^{1}/_{2} sin4\theta_Z} \end{aligned} \tag{9}$$

and the relative phase introduced between the slow and the fast replica, $\phi_{G_s - G_f}$, is

$$\phi_{G_s - G_f}(\theta_Z, {}^{\pi}/_{2}) = arctan({}^{sin2\theta_Z}/_{\cos^2 2\theta_Z}) \tag{10}$$

The amplitude and phase modulations of Eqs. (9) and (10) are plotted in Fig. 2 (dashed lines). In this case, there is a variation of the amplitude of the pulse replicas, with ZWP positions with balanced amplitude ($|G_f| = |G_s| = 0.5$, for $\theta_Z = m \cdot 45°$ being m an integer, where the QWP preserves the input linear polarization or coverts it to circular polarization) and positions with fast and slow replica amplitude modulation up to roughly +22% and −29% (with respect to that balance) in the intermediate polarization, for $\theta_Z = 22.5° + m \cdot 45°$, which corresponds to a maximum contrast of 42% as defined before. Regarding the relative phase between the pulse replicas, $\phi_{G_s - G_f}$ (see Eq. (8)), its value is $\pm\pi/2$ (QWP creates right- or left-handed circular polarization) or 0 (preserved linear polarization) when the amplitude of the replicas is balanced, i.e. $|G_f| = |G_s|$, while for the positions with the highest contrast between $|G_f|$ and $|G_s|$, the value of $\phi_{G_s - G_f}$ is $\pm 0.30\pi$. In intermediate positions, the phase $\phi_{G_s - G_f}$ varies between $\pm\pi/2$ (see Fig. 2). Please remember that this phase is added to the phase retardation due to the later static MWP. Thus, recalling the study done in a previous work dealing with the performance of the amplitude technique [27], where it was shown there that the original amplitude swing was valid for any value of the phase retardation of the MWP, here it suggests that this phase variation can also help in the task of encoding the pulse phase. Therefore, in this case the amplitude modulation is interpreted as corresponding to a variation of the relative amplitude of the replicas, combined with a variation of their relative phase. The trace can be interpreted as several portions of conventional amplitude swing traces, in the area around the amplitude balance of the replica, with many different phase retardations.

2.2. Numerical study of the performance of different modulations

Before, we have presented the analytical study of new configurations of amplitude swing based on a rotating ZWP before a fixed MWP, and we have compared some features with the original amplitude swing configuration (rotating MWP).

Now, we compare the robustness against noise of various configurations simulating and reconstructing different amplitude swing traces for four configurations: rotating MWP, rotating HWP with fixed MWP, rotating QWP with fixed MWP and rotating ZWP of $\phi_r = 0.75\pi$ with fixed MWP, being the fixed MWP always at $\theta_M = 45°$, as described in the previous section. All configurations presented here use the same MWP (either rotating or static), a 2-mm-thick quartz with $\phi_M = \pi$ phase retardation, which introduces a 60-fs delay at 800 nm.

Here we present the analysis of a pulse with gaussian spectrum centred at 800 nm with 50-fs Fourier-limit duration (FWHM) and a spectral phase that is the sum of a $GDD = 1000\ \text{fs}^2$, a

TOD = 2000 fs^3, and an oscillatory term given by $0.3\pi \cdot cos\,[50\,(\omega - \omega_0) + 0.25\pi]$, where ω_0 is the central angular frequency of the spectrum (measured in units of rad/fs).

To study the behaviour of the different configurations against various noise levels, the ideal amplitude swing traces for each configuration have been simulated and different white Gaussian noise levels (defined as the root mean square (rms) of the noise with respect to the normalized trace) from 0 to 15% have been added to them. The traces are reconstructed using the algorithm described in the Appendix A (Section 4.3). In this example, for the optimization we use a logarithmic merit function to compare the noisy simulated trace and the retrieved trace.

An example with a noise level of 4.3% rms is illustrated in Fig. 4, where the four studied configurations are shown in different columns. Results for other noise levels in said range are shown in Visualization 10. Figure 4(a,c) correspond to the ideal, noisy and retrieved amplitude swing traces, respectively. From this representation, it can be observed that the agreement of the retrieved and ideal traces is good, even with the high noise level of the simulated traces analysed with the algorithm, Fig. 4(b). The good agreement is also observed in the spectral and temporal intensity and phase comparison depicted in Fig. 4(d,e), respectively, where the theoretical dependences are shown in gray lines. The temporal intensity of the pulses is normalized to the peak intensity of the simulated pulse, for the later comparison (instead of normalizing the retrieved pulse too, in this way we take into account the energy of the pulse that extends outside the main peak of the reconstruction).

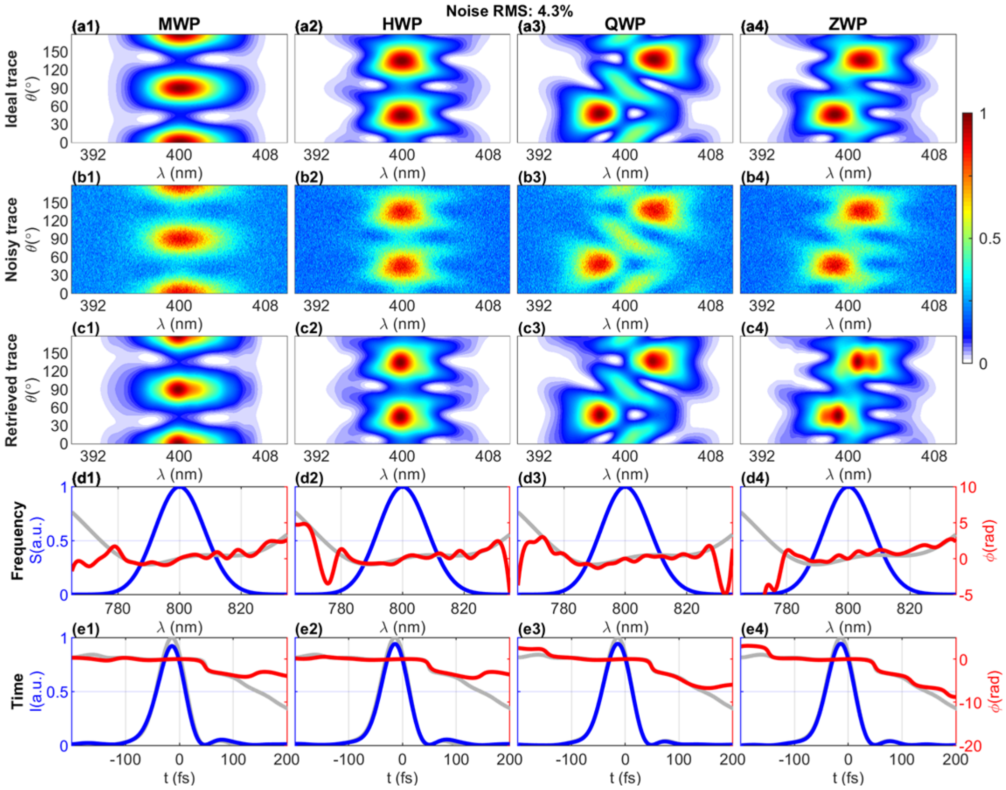

Fig. 4. Comparison of amplitude swing configurations analysing traces with 4.3% rms noise added. (a) Ideal, (b) noisy and (c) retrieved amplitude swing traces. (d) Spectral and (e) temporal comparison of the retrieved (blue and red) and theoretical (gray) pulses. The configurations studied are: (column 1) rotating MWP, (column 2) rotating HWP, (column 3) rotating QWP, and (column 4) rotating ZWP $\phi_r = 0.75\pi$.

Apart from the graphical qualitative evaluation of the results, we propose some quantitative comparisons that can be taken into account to assess the robustness for different noise levels and different amplitude swing configurations (Fig. 5). Firstly, Fig. 5(a) represents the rms between the ideal and retrieved traces (solid lines) for different noise levels using the four configurations. Notice that we compare the retrieved trace with the ideal one, instead of the noisy trace, because it gives a better quantification of the quality of the retrieval. In addition, Fig. 5(a) also includes the rms between the temporal intensities (dashed lines) of the ideal pulse used to simulate the traces and the retrieved pulse from the noisy trace. Also, the retrieved temporal pulse duration (FWHM) of each case is compared with the theoretical value of 57.7 fs (dashed gray line) in Fig. 5(b).

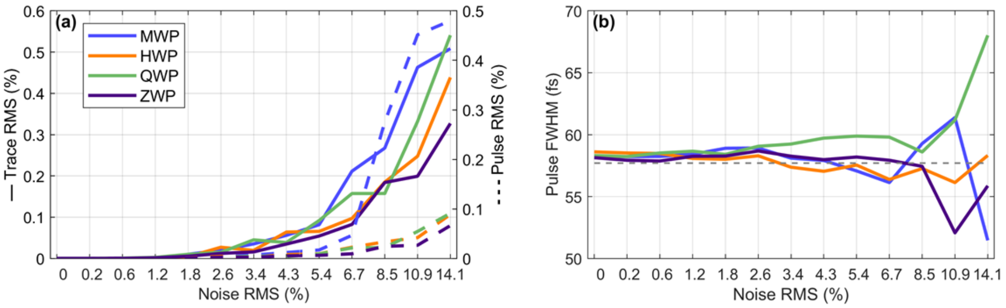

Fig. 5. Comparison of (a) rms between the ideal and retrieved amplitude swing traces (solid lines, left scale) and temporal intensities (dashed lines, right scale), and (b) pulse duration (FWHM) for different noise levels. The amplitude swing configurations are: (blue) rotating MWP, (orange) rotating HWP, (green) rotating QWP, and (purple) rotating ZWP with $\phi_r = 0.75\pi$. The theoretical FWHM (dashed gray line) is depicted in (b).

From the analysis of the example presented here we find that all configurations provide a good pulse reconstruction even for high noise levels (∼5%). If we analyse higher noise values, all the new configurations (generalizing amplitude swing modulation) are slightly better than the original amplitude swing (rotating MWP), with a better performance of the rotating ZWP with $\phi_r = 0.75\pi$.

Nevertheless, this is a single example, and the behaviour may change depending on the pulse under study, the phase retardation of the MWP, the merit function used for the optimizations and the retrieval algorithm itself. For this reason, we performed the same kind of simulations and reconstructions under different conditions (see details in Supplement 1, Section 5). Firstly, we repeated the previous example but only changing the phase retardation to $\phi_M = 0$ and 0.4π (Supplementary Fig. S8-S9 and S10-S11, and Visualization 11 and Visualization 12, respectively). Then, with respect to the last case of $\phi_M = 0.4\pi$, we only changed the merit function to the absolute value of the difference between the traces and repeated the complete analysis (Supplementary Fig. S12-S13 and Visualization 13). Finally, we repeated the study with a different pulse, with the same spectrum but the spectral phase corresponding having a $GDD = 4000$ fs^2 and a $TOD = 200000$ fs^3 (pulse duration of 86.9 fs, FWHM), the MWP phase retardation being $\phi_M = 0.7\pi$ and using the absolute difference of the traces as merit function (results in Supplementary Fig. S14-S15 and Visualization 14).

From a complete analysis of said examples, we can extract the following conclusions. First, depending on the specific case one configuration may be better than the others, there is not a general rule since it depends on the situation parameters, as explained before. Even so, one general feature that we have observed simulating different situations is that, for low and moderate noise levels, all configurations present good convergence. Indeed, the noise levels in which some differences can be observed are remarkably high and, if they are present in experimental measurements, they are usually considered as too high, and some other experimental strategies are taken to improve the signal to noise ratio.

2.3. Experimental measurements

In this section we present the experimental demonstration of different amplitude swing configurations. We used it to study an almost compressed pulse and a chirped one, both with different amplitude swing configurations. The pulse spectrum is centred at 798 nm and has a Fourier-transform limit pulse duration of 56-fs (FWHM).

Here, the pulses were characterized using three different configurations of amplitude swing. All of them were implemented using the same MWP (delay between replicas of 60 fs). One configuration was the original amplitude swing [26] based on a rotating MWP. The other two configurations were based on a rotating ZWP before a fixed MWP at 45° as introduced before (see the experimental setup description in Section 2.1 and Fig. 1). Playing the role of ZWP, we have used an achromatic HWP and QWP, respectively. More experimental details can be found in the Appendix A, as well as for the algorithm we used to reconstruct the pulses from the traces.

Figure 6 depicts the amplitude swing experimental (columns 1 and 3) and retrieved (columns 2 and 4) traces for the characterization of a nearly compressed (columns 1 and 2) and a chirped (columns 3 and 4) pulse. Figure 6(a) shows the traces for the conventional amplitude swing configuration, whereas Fig. 6(b,c) depict the traces for the rotating HWP and QWP, respectively. Notice that the convergence is good for all the strategies showing rms differences between the experimental and retrieved traces lower than 0.12%.

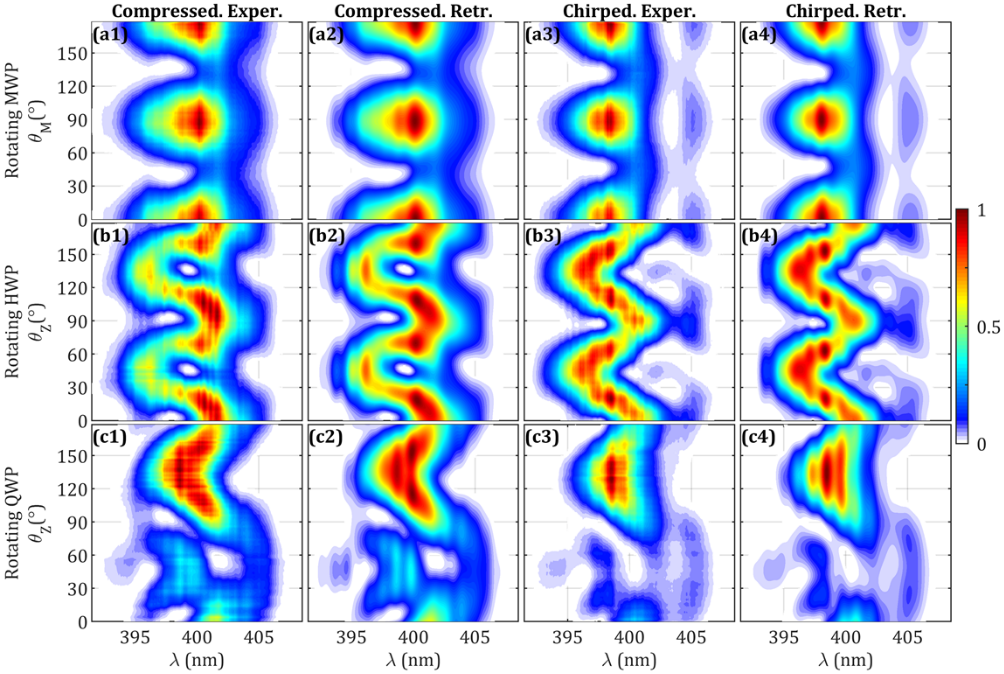

Fig. 6. Amplitude swing trace with rotating MWP (row a), rotating HWP and static MWP (row b), rotating QWP and static MWP (row c). It features experimental (columns 1,3) and retrieved (columns 2,4) traces. Concerning the pulse characteristics, it has been considered compressed (columns 1,2) and chirped (columns 3,4) pulse cases.

The retrieved pulses with the different amplitude swing configurations are shown in Fig. 7(a,c) for the compressed pulse and Fig. 7(b,d) for the chirped pulse. The gray shaded areas in the retrievals correspond to the standard deviation from the mean phase of each retrieval with the 3 configurations in the spectral and temporal domains. The measurement with the conventional scheme (rotating MWP) can be used to validate the new configurations of amplitude swing (rotating HWP and QWP, in this experiment).

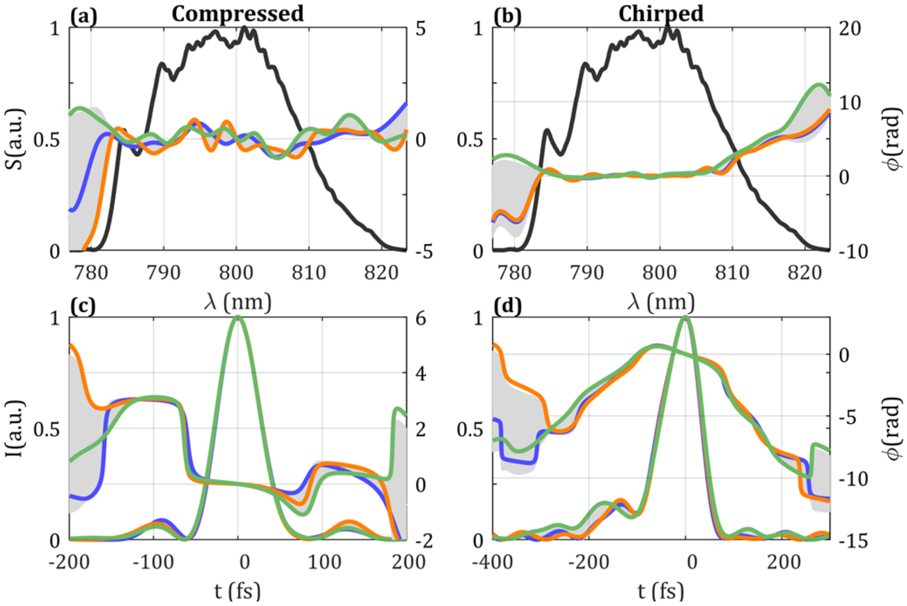

Fig. 7. (a,b) Experimental spectrum (black) and retrieved spectral phase, (c,d) retrieved temporal intensity and phase. (a,c) Unchirped and (b,d) chirped pulses. Retrievals for amplitude swing trace with rotating MWP (blue), rotating HWP and static MWP (orange), rotating QWP and static MWP (green). Gray shaded areas represent the standard deviation from the mean of each retrieval with the 3 configurations.

Regarding the spectral comparison, Fig. 7(a,b), the retrievals present the same spectral phases in each situations (compressed and chirped pulse), regardless the amplitude swing configuration used. This good agreement is also observed in the temporal intensity and phase (Fig. 7(c,d)) and the temporal duration (FWHM) for each pulse. The retrieved pulse durations (FWHM) for the compressed pulse are: 57.0 fs with the rotating MWP, 57.4 fs the rotating HWP and 57.3 fs the rotating QWP (mean value 57.2 ± 0.2 fs). The retrieved temporal FWHM durations for the chirped pulse also agree between them: 93.4 fs with the rotating MWP, 93.2 fs the rotating HWP and 93.0 fs the rotating QWP (mean value 93.2 ± 0.2 fs).

3. Discussion and conclusions

We have introduced a generalization of the pulse replicas modulation in the amplitude swing technique for the measurement of ultrashort laser pulses. The modulation pattern consists in imparting different relative amplitudes and phases to the pulse replicas that interfere to encode the pulse information. The experimental implementation of the pulse manipulation is direct, and it is done with in-line interferometers (standard interferometers would require careful alignment and they present instabilities). We have analysed different configurations rotating zero-order waveplates before a static multiple-order waveplate and the second-harmonic generation. We have explored theoretically the pulse modulation for diverse retardations (general case, half-wave and quarter-wave retardation) of the zero-order waveplate, quantifying the amplitude and phase variations in terms of contrast and relative phase excursion between the replicas along a measured trace, and compared it to the conventional implementation of amplitude swing. From this, we find that phase retardations between $\pi/2$ and $3\pi/2$ are suitable for the pulse measurement, while extreme cases close to zero or complete wave retardation does not sufficiently modulate the replicas. Through the numerical calculations, we have investigated its influence on the pulse reconstruction, finding that in the studied cases the proposed configuration can encode the pulse phase in a more robust way for relevant noise levels in the measurements, allowing the appropriate reconstruction of the pulses under more adverse conditions, as for example unstable pulse energy or low-signal lasers. As a key result, we conclude that the amplitude and phase modulation can be generalized while keeping the pulse phase encoded and allowing pulse reconstruction, being the amplitude swing concept generalized.

The configurations proposed here are simple and can be readily interpreted. Nonetheless, other configurations are also possible. For example, we have shown here the reconstruction with input linear polarization for the pulse replicas manipulation, but other input polarizations (e.g., linear at other orientation, or even circular or elliptical polarization) would lead to a similar phase encoding and conclusions. Also, other analogous schemes could be used instead, e.g., rotating the zero-order waveplate after the multiple-order waveplate or combining two multiple-order waveplates. Regarding the zero-order waveplate, we have assumed it to be achromatic, but this is not a requirement if its dispersion is well known, which may aid in the measurement of ultrabroadband pulses.

From a practical aspect, the work proposed here may also benefit the pulse reconstruction with amplitude swing in the following manner. For example, in the case that the multiple-order waveplate cannot be easily rotated, e.g., when using several multiple-order waveplate or a pair of birefringent wedges to adjust the delay between the replicas (notice that the delay must be of the order of the Fourier-transform limit of the pulse spectrum, finding completely reliable reconstructions up to a factor 3 greater or less), where rotating these elements can be awkward or unrealistic, the configuration shown here solves the limitation and allows applying the measurement. Another advantage is that with the same setup (and a single multiple-order waveplate), different schemes can be applied to perform the amplitude swing measurement, just adding, e.g., a half- or quarter-waveplate (commonly available in the laboratory). Therefore, several individual measurements can be taken (in general, this is not possible with other techniques [5,31], at least without introducing major variations), from which their retrievals can be compared, so that it confers more robustness to the pulse characterization. This has been shown and validated experimentally here with the reconstruction of ultrashort pulses using three different configurations.

Altogether, considering the versatility, robustness and simplicity of the technique, which can be applied to different spectral ranges and to different temporal durations of the pulses, we expect that the modulation proposed here will help the community users of ultrafast lasers in the characterization of laser pulses.

4. Appendix A: description of the methods

4.1 Experimental details

The laser system used in this experiment was a Titanium:sapphire CPA laser (Spectra-Physics, model Spitfire ACE) that provides pulses centred at 798 nm with a Fourier-limit duration of 56-fs and a repetition rate of 5 kHz. The grating-based compressor of this system allows to modify the output pulse GDD, thus generating compressed or chirped pulses.

As MWP, we used a 2-mm-thick quartz plate, which introduces a delay between replicas of around 60 fs and has a phase retardation of 0.34π at 800 nm. The phase retardation of the MWP was accurately calibrated with in-line interferometry [32]. The HWP and QWP (from Eksma Optics) can be considered achromatic in the bandwidth of the pulse. The SHG medium was a 20-µm Type-I BBO with perfect phase-matching for the pulse bandwidth. A polarizing cube was used to separate the fundamental signal from the SHG. The SHG signal was measured with a spectrometer (HR4000 from Ocean Optics Inc.) for different orientations of the retarder plates and the fundamental spectrum was measured before the amplitude swing system using another spectrometer (AvaSpec 2048-USB1 from Avantes Inc.).

4.2 Models used in the simulations

In the simulations, the pulse is firstly represented by its amplitude and phase in the spectral domain. Then, the effect of the modulating elements (MWP, ZWP and LP) is calculated for different orientations of the retarder plates, which includes using Jones calculus. The dispersion of those elements is calculated from their material and thickness using Sellmeier equations. After that, by Fourier-transforming, the pulse is calculated in the temporal domain, where it is squared to model the SHG process (see Eqs. (1) and (2)). Finally, from that, it is calculated the spectrum of the SHG, which gives the corresponding amplitude swing traces.

4.3 Data analysis for pulse reconstruction

In order to reconstruct pulses from the amplitude swing traces, we used the experimental spectrum of the pulse and calculate the spectral phase encoded in the measured SHG trace. This kind of phase retrieval in a nonlinear trace is a multi-parameter problem since the phase is a function. To solve it, we parametrize this function and apply the Levenberg-Marquardt nonlinear optimization algorithm, which has been used before reconstruction dispersion scan [33,34] and amplitude swing [26,27] traces. The phase parametrization can be done in different ways, e.g., series expansions or discretization. Here, the phase is parametrized as the combination of GDD and TOD parameters, added to the derivative of the phase in 24 equispaced spectral points (from these values, the phase is integrated and interpolated in the frequency axis). The algorithm has been upgraded to include the shaping elements that perform the amplitude swing modulation presented in this work. The dispersion of the different elements —e.g., the MWP, the ZWP (HWP or QWP) and the LP— is considered within the reconstruction algorithm so that the input pulse is retrieved. The strategy followed by the algorithm consists in starting from a guess pulse phase (arbitrary, e.g., random or flat phase), calculating the SHG trace from it, and comparing it to the experimental one (using a merit function). The unknown parameters that represent the phase discretization are varied while calculating the simulated trace, and they are varied in a gradient-based strategy to reduce the merit function. The convergence is reached when the merit function is below a given threshold or when a defined number of iterations is reached. At this point, the spectral phase is retrieved, so that the amplitude and phase of the pulse is reconstructed in the spectral and the temporal domain. The merit function can be defined in different ways to improve the reconstruction: a very extended way is to use the rms, but here we also use the absolute difference of the traces, or the absolute difference of the logarithm of the traces (normalized and comparing down to a certain threshold that we chose to be 1.5 orders of magnitude). The last two help on the reconstruction to retrieve the low-level signal parts of the traces that come from the pulse replica interferences.

Funding. European Regional Development Fund; Consejería de Educación, Junta de Castilla y León (SA136P20); Ministerio de Ciencia e Innovación (PID2020-119818GB-I00); Ministerio de Economía y Competitividad (EQC2018-004117-P, FIS2017-87970-R).

Disclosures. IJS: Universidad de Salamanca (P), BA: Universidad de Salamanca (P).

Data availability. Data underlying the results presented in this paper are not publicly available at this time but may be obtained from the authors upon reasonable request.

Supplemental document. See Supplement 1 for supporting content.

References

1. W. Watanabe, Y. Li, and K. Itoh, "[INVITED] Ultrafast laser micro-processing of transparent material," Opt. Laser Technol. **78**, 52–61 (2016).
2. C. Xu and F. W. Wise, "Recent advances in fibre lasers for nonlinear microscopy," Nat. Photonics **7**(11), 875–882 (2013).
3. R. Stoian and J. P. Colombier, "Advances in ultrafast laser structuring of materials at the nanoscale," Nanophotonics **9**(16), 4665–4688 (2020).
4. G. Buchberger, M. Muck, C. Plamadeala, and J. Heitz, "*Laser Structuring for Biomedical Applications*," in (Springer, Cham, 2023), pp. 1105–1165.
5. I. A. Walmsley and C. Dorrer, "Characterization of ultrashort electromagnetic pulses," Adv. Opt. Photon. **1**(2), 308–437 (2009).
6. G. Stibenz, C. Ropers, C. Lienau, C. Warmuth, A. S. Wyatt, I. A. Walmsley, and G. Steinmeyer, "Advanced methods for the characterization of few-cycle light pulses: A comparison," Appl. Phys. B **83**(4), 511–519 (2006).
7. J. A. Armstrong, "Measurement of picosecond laser pulse widths," Appl. Phys. Lett. **10**(1), 16–18 (1967).
8. C. Iaconis and I. A. Walmsley, "Spectral phase interferometry for direct electric-field reconstruction of ultrashort optical pulses," Opt. Lett. **23**(10), 792–794 (1998).
9. D. J. Kane and R. Trebino, "Characterization of Arbitrary Femtosecond Pulses Using Frequency-Resolved Optical Gating," IEEE J. Quantum Electron. **29**(2), 571–579 (1993).
10. T. Oksenhendler, S. Coudreau, N. Forget, V. Crozatier, S. Grabielle, R. Herzog, O. Gobert, and D. Kaplan, "Self-referenced spectral interferometry," Appl. Phys. B **99**(1-2), 7–12 (2010).
11. V. V. Lozovoy, I. Pastirk, and M. Dantus, "Multiphoton intrapulse interference IV Ultrashort laser pulse spectral phase characterization and compensation," Opt. Lett. **29**(7), 775–777 (2004).
12. M. Miranda, C. L. Arnold, T. Fordell, F. Silva, B. Alonso, R. Weigand, A. L'Huillier, and H. Crespo, "Characterization of broadband few-cycle laser pulses with the d-scan technique," Opt. Express **20**(17), 18732–18743 (2012).
13. J.-C. M. Diels, J. J. Fontaine, I. C. McMichael, and F. Simoni, "Control and measurement of ultrashort pulse shapes (in amplitude and phase) with femtosecond accuracy," Appl. Opt. **24**(9), 1270–1282 (1985).
14. B. Kohler, J. Squier, K. W. DeLong, R. Trebino, V. V. Yakovlev, and K. R. Wilson, "Phase and intensity characterization of femtosecond pulses from a chirped-pulse amplifier by frequency-resolved optical gating," Opt. Lett. **20**(5), 483–485 (1995).
15. E. M. Kosik, A. S. Radunsky, I. A. Walmsley, and C. Dorrer, "Interferometric technique for measuring broadband ultrashort pulses at the sampling limit," Opt. Lett. **30**(3), 326–328 (1995).
16. A. Tajalli, B. Chanteau, M. Kretschmar, H. G. Kurz, D. Zuber, M. Kovačev, U. Morgner, and T. Nagy, "Few-cycle optical pulse characterization via cross-polarized wave generation dispersion scan technique," Opt. Lett. **41**(22), 5246–5249 (2016).
17. I. Sytcevich, C. Guo, S. Mikaelsson, J. Vogelsang, A.-L. Viotti, B. Alonso, R. Romero, P. T. Guerreiro, Í. J. Sola, A. L'Huillier, H. Crespo, M. Miranda, and C. L. Arnold, "Characterizing ultrashort laser pulses with second harmonic dispersion scans," J. Opt. Soc. Am. B **38**(5), 1546–1555 (2021).
18. S. B. Park, K. Kim, W. Cho, S. I. Hwang, I. Ivanov, C. H. Nam, and K. T. Kim, "Direct sampling of a light wave in air," Optica **5**(4), 402–408 (2018).
19. A. Korobenko, K. Johnston, M. Kubullek, L. Arissian, Z. Dube, T. Wang, M. Kübel, A. Y. Naumov, D. M. Villeneuve, M. F. Kling, P. B. Corkum, A. Staudte, and B. Bergues, "Femtosecond streaking in ambient air," Optica **7**(10), 1372–1376 (2020).
20. J. R. Birge, R. Ell, and F. X. Kärtner, "Two-dimensional spectral shearing interferometry for few-cycle pulse characterization," Opt. Lett. **31**(13), 2063–2065 (2006).
21. B. Xu, J. M. Gunn, J. M. Dela Cruz, V. V. Lozovoy, and M. Dantus, "Quantitative investigation of the multiphoton intrapulse interference phase scan method for simultaneous phase measurement and compensation of femtosecond laser pulses," J. Opt. Soc. Am. B **23**(4), 750–759 (2006).
22. M. Canhota, F. Silva, R. Weigand, and H. M. Crespo, "Inline self-diffraction dispersion-scan of over octave-spanning pulses in the single-cycle regime," Opt. Lett. **42**(15), 3048–3051 (2017).
23. Ó. Pérez-Benito and R. Weigand, "Nano-dispersion-scan: measurement of sub-7-fs laser pulses using second-harmonic nanoparticles," Opt. Lett. **44**(20), 4921–4924 (2019).
24. W. Cho, S. I. Hwang, C. H. Nam, M. R. Bionta, P. Lassonde, B. E. Schmidt, H. Ibrahim, F. Légaré, and K. T. Kim, "Temporal characterization of femtosecond laser pulses using tunneling ionization in the UV, visible, and mid-IR ranges," Sci. Rep. **9**(1), 16067 (2019).
25. A. S. Johnson, E. B. Amuah, C. Brahms, and S. Wall, "Measurement of 10 fs pulses across the entire Visible to Near-Infrared Spectral Range," Sci. Rep. **10**(1), 4690 (2020).
26. B. Alonso, W. Holgado, and Í. J. Sola, "Compact in-line temporal measurement of laser pulses with amplitude swing," Opt. Express **28**(10), 15625–15640 (2020).
27. Í. J. Sola and B. Alonso, "Robustness and capabilities of ultrashort laser pulses characterization with amplitude swing," Sci. Rep. **10**(1), 18364 (2020).
28. M. López-Ripa, Í. J. Sola, and B. Alonso, "Amplitude swing ultrashort pulse characterization across visible to near-infrared," Opt. Laser Technol. **164**, 109492 (2023).

29. C. Barbero, B. Alonso, and Í. J. Sola, "Retrieving Ultrashort Pulses with Time-Varying Polarization Using Amplitude Swing," SSRN, SSRN:4443101 (2023).
30. M. López-Ripa, Í. J. Sola, and B. Alonso, "Bulk lateral shearing interferometry for spatiotemporal study of time-varying ultrashort optical vortices," Photonics Res. **10**(4), 922–931 (2022).
31. M. Miranda, T. Fordell, C. Arnold, A. L'Huillier, and H. Crespo, "Simultaneous compression and characterization of ultrashort laser pulses using chirped mirrors and glass wedges," Opt. Express **20**(1), 688–697 (2012).
32. B. Alonso and Í. Sola, "Measurement of Ultrashort Vector Pulses From Polarization Gates by In-Line, Single-Channel Spectral Interferometry," IEEE J. Select. Topics Quantum Electron. **25**(4), 8900307 (2019).
33. F. Silva, B. Alonso, W. Holgado, R. Romero, J. S. Román, E. C. Jarque, H. Koop, V. Pervak, H. Crespo, and Í. J. Sola, "Strategies for achieving intense single-cycle pulses with in-line post-compression setups," Opt. Lett. **43**(2), 337–340 (2018).
34. B. Alonso, Í. J. Sola, and H. Crespo, "Self-calibrating d-scan: Measuring ultrashort laser pulses on-target using an arbitrary pulse compressor," Sci. Rep. **8**(1), 3264 (2018).